Cell Reports

The histone H3K9M mutation synergizes with H3K14 ubiquitylation to selectively sequester histone H3K9 methyltransferase Clr4 at heterochromatin

Graphical abstract

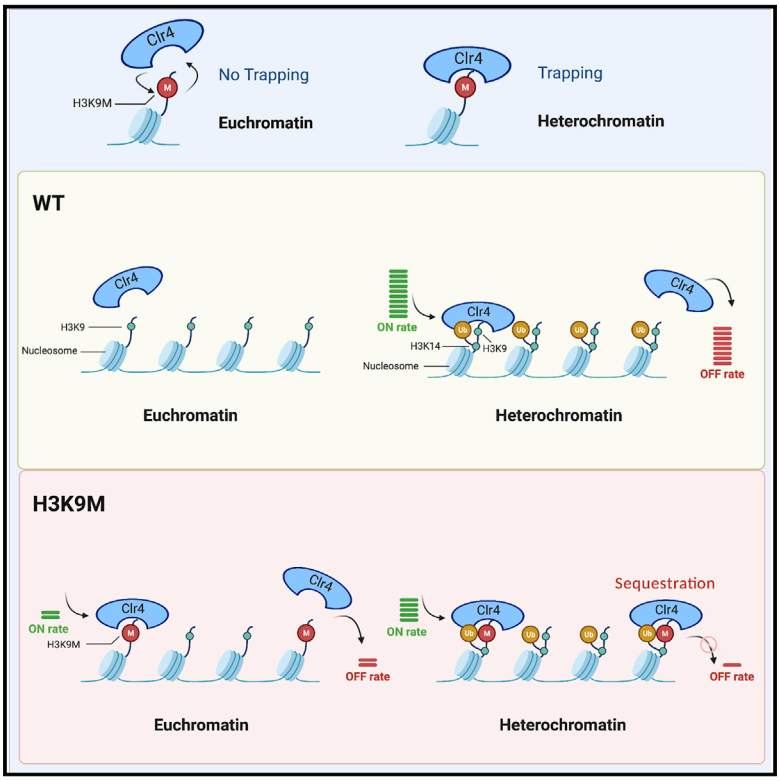

Highlights

- Clr4 is selectively sequestered by H3K9M at heterochromatin
- H3K14ub synergizes with H3K9M to sequester Clr4 at heterochromatin *in vivo*
- H3K14ub synergizes with H3K9M to promote interaction with Clr4 *in vitro*
- H3K14ub changes the kinetics of the H3K9M-Clr4 interaction

Authors

Chun-Min Shan, Jin-Kwang Kim, Jiyong Wang, ..., Liang Tong, Feng Qiao, Songtao Jia

Correspondence

sj2274@columbia.edu

In brief

Shan et al. report that the selective sequestration of the H3K9 methyltransferase Clr4 by H3K9M at heterochromatin requires an additional histone modification, H3K14ub. *In vitro* characterization reveals that H3K14ub changes the kinetics of the Clr4-H3K9M interaction. This selective sequestration model reconciles previous discrepancies on the mechanism of histone lysine-to-methionine mutations.

Shan et al., 2021, Cell Reports *35*, 109137
May 18, 2021
https://doi.org/10.1016/j.celrep.2021.109137

CellPress

Cell Reports

CellPress
OPEN ACCESS

Report

The histone H3K9M mutation synergizes with H3K14 ubiquitylation to selectively sequester histone H3K9 methyltransferase Clr4 at heterochromatin

Chun-Min Shan,[1] Jin-Kwang Kim,[2] Jiyong Wang,[1,10] Kehan Bao,[1] Yadong Sun,[1,11] Huijie Chen,[3] Jia-Xing Yue,[4,12] Alessandro Stirpe,[5,13] Zhiguo Zhang,[6,7,8,9] Chao Lu,[7,9] Thomas Schalch,[5] Gianni Liti,[4] Peter L. Nagy,[3,14] Liang Tong,[1] Feng Qiao,[2] and Songtao Jia[1,15,*]

[1]Department of Biological Sciences, Columbia University, New York, NY 10027, USA
[2]Department of Biological Chemistry, School of Medicine, University of California, Irvine, Irvine, CA 92697, USA
[3]Department of Pathology, Columbia University, New York, NY 10068, USA
[4]Université Côte d'Azur, CNRS, INSERM, IRCAN, Nice 06107, France
[5]Leicester Institute for Structural and Chemical Biology, Department of Molecular and Cell Biology, University of Leicester, Leicester LE1 9HN, UK
[6]Institute for Cancer Genetics, Columbia University Irving Medical Center, New York, NY 10032, USA
[7]Herbert Irving Comprehensive Cancer Center, Columbia University Irving Medical Center, New York, NY 10032, USA
[8]Department of Pediatrics, Columbia University Irving Medical Center, New York, NY 10032, USA
[9]Department of Genetics and Development, Columbia University Irving Medical Center, New York, NY 10032, USA
[10]Present address: Greenwood Genetic Center, Greenwood, SC 29646, USA
[11]Present address: School of Life Science and Technology, ShanghaiTech University, Shanghai 201210, China
[12]Present address: State Key Laboratory of Oncology in South China, Collaborative Innovation Center for Cancer Medicine, Sun Yat-Sen University Cancer Center, Guangzhou 510060, China
[13]Present address: Wellcome Center for Cell Biology, School of Biological Sciences, The University of Edinburgh, Edinburgh EH9 3BF, UK
[14]Present address: Praxis Genomics, LLC, Atlanta, GA 30328, USA
[15]Lead contact
*Correspondence: sj2274@columbia.edu
https://doi.org/10.1016/j.celrep.2021.109137

SUMMARY

Oncogenic histone lysine-to-methionine mutations block the methylation of their corresponding lysine residues on wild-type histones. One attractive model is that these mutations sequester histone methyltransferases, but genome-wide studies show that mutant histones and histone methyltransferases often do not colocalize. Using chromatin immunoprecipitation sequencing (ChIP-seq), here, we show that, in fission yeast, even though H3K9M-containing nucleosomes are broadly distributed across the genome, the histone H3K9 methyltransferase Clr4 is mainly sequestered at pericentric repeats. This selective sequestration of Clr4 depends not only on H3K9M but also on H3K14 ubiquitylation (H3K14ub), a modification deposited by a Clr4-associated E3 ubiquitin ligase complex. *In vitro*, H3K14ub synergizes with H3K9M to interact with Clr4 and potentiates the inhibitory effects of H3K9M on Clr4 enzymatic activity. Moreover, binding kinetics show that H3K14ub overcomes the Clr4 aversion to H3K9M and reduces its dissociation. The selective sequestration model reconciles previous discrepancies and demonstrates the importance of protein-interaction kinetics in regulating biological processes.

INTRODUCTION

Recent sequencing analyses have found that histone lysine-to-methionine mutations are associated with distinct types of cancers. For example, more than 80% of diffuse intrinsic pontine gliomas contain a somatic K27M mutation in histone H3.3 or H3 (Schwartzentruber et al., 2012; Sturm et al., 2012; Wu et al., 2012), and more than 90% of chondroblastomas and a subset of head and neck squamous cell carcinomas contain a K36M mutation in histone H3.3 or H3 (Behjati et al., 2013; Papillon-Cavanagh et al., 2017). These mutations transform normal cells into tumor-like states, suggesting that they have critical roles in tumorigenesis (Chan et al., 2013a; Fang et al., 2016; Funato et al., 2014; Lu et al., 2016; Mohammad et al., 2017).

Introducing histones containing lysine-to-methionine mutations, such as H3K9M, H3K27M, and H3K36M, into mammalian or yeast cells all reduced methylation of their corresponding lysine residues on wild-type histones (Brumbaugh et al., 2019; Chan et al., 2013a, 2013b; Fang et al., 2016; Herz et al., 2014; Lewis et al., 2013; Lu et al., 2016; Mohammad et al., 2017; Piunti et al., 2017; Sarthy et al., 2020; Shan et al., 2016; Stafford et al., 2018; Zhang et al., 2017), suggesting that they function in a

dominant fashion and, possibly, through similar mechanisms. One of the most attractive models through which these mutations regulate global histone methylation is the sequestration of histone methyltransferases. Such a hypothesis is supported by interaction assays showing that K-to-M mutations enhanced the binding between histones and their methyltransferases both *in vitro* and *in vivo* (Bender et al., 2013; Chan et al., 2013a; Fang et al., 2016; Jayaram et al., 2016; Justin et al., 2016; Lu et al., 2016; Shan et al., 2016; Zhang et al., 2017). However, recent studies of the H3.3K27M mutation *in vivo* are not entirely consistent with the sequestration model. For example, chromatin immunoprecipitation sequencing (ChIP-seq) analyses of cancer cells expressing H3.3K27M found that, although the H3K27 methyltransferase PRC2 levels are higher at a set of poised enhancers that also contains H3.3K27M, most genomic loci containing high levels of H3.3K27M show no association with PRC2 (Fang et al., 2018; Piunti et al., 2017; Sarthy et al., 2020). Moreover, mass spectrometry analyses of proteins associated with H3.3K27M-containing nucleosomes did not detect higher levels of PRC2 than wild-type nucleosomes did (Herz et al., 2014). It is, therefore, critical to resolve these discrepancies to better understand the function of these mutations in tumorigenesis.

We have previously established a model of the H3K9M mutation in fission yeast (Shan et al., 2016). In this organism, histone H3K9 methylation is required for the formation of heterochromatin at repetitive DNA elements (Grewal and Jia, 2007), and there are three copies of the histone H3 genes (*hht1*$^+$, *hht2*$^+$, and *hht3*$^+$) with identical protein sequences. We have generated FLAG-tagged versions of wild-type and K9M mutant at the endogenous *hht3*$^+$ locus. Western blot analysis with a histone H3 antibody indicates that the mutant histone is expressed at lower levels than endogenous histone H3 is (Figure 1A). We found that H3K9M dominantly blocks H3K9 methylation at major heterochromatin domains (Shan et al., 2016). Moreover, the H3K9M mutation enhances the interaction between the H3K9 methyltransferase Clr4 and histone H3 tail peptide *in vitro*, and that mutation results in higher levels of Clr4 at heterochromatin *in vivo*, leading to a model of H3K9M sequestering Clr4 to block H3K9 methylation (Shan et al., 2016).

In this study, we used that fission yeast H3K9M model to further examine whether the H3K9M mutation functions through the sequestration of Clr4. We found that, even though the H3K9M mutant histone is broadly distributed across the genome, Clr4 is only sequestered at heterochromatin, suggesting that additional mechanisms at heterochromatin might facilitate the sequestration of Clr4 by H3K9M. Clr4 associates with an E3 ubiquitin ligase complex, composed of Cul4, Rik1, Raf1, and Raf2 (Hong et al., 2005; Horn et al., 2005; Jia et al., 2005), to form CLRC. CLRC ubiquitylates histone H3K14 (H3K14ub), and H3K14ub is associated with H3K9me3 containing heterochromatin, but not H3K4me3 containing euchromatin (Oya et al., 2019; Stirpe et al., 2020). We found that mutating either CLRC or H3K14 abolished the sequestration of Clr4 by H3K9M. Furthermore, we show that *in vitro*, H3K9M works synergistically with H3K14ub to interact with Clr4, and H3K14ub potentiates the inhibitory effects of H3K9M. These results demonstrate that H3K14ub is critical for the sequestration of Clr4 by H3K9M.

RESULTS AND DISCUSSION

To further examine the mechanism by which H3K9M functions, we performed ChIP-seq analyses of Hht3-K9M and Clr4 (Figure 1B). In wild-type cells, Hht3 is broadly distributed across the genome, with the only exception being at the centromeric regions, in which histone H3 is replaced with a histone-variant CENP-A. Clr4 is mainly localized at pericentric regions, where many repetitive elements are present and H3K9me3 levels are high (Figure 1A). The localization pattern of Hht3-K9M is similar to that of wild-type Hht3 (Figure 1A), indicating that the mutation has little effect on the incorporation of histone H3 into chromatin. In *hht3-K9M* cells, Clr4 is still mainly enriched at pericentric repeats but with higher levels than found in wild-type cells (Figure 1B). ChIP-qPCR analyses of Clr4 and H3, using a strain expressing FLAG-Clr4 and Hht3-GFP, confirm that Clr4 levels increase at pericentric *dh* repeats, but not at euchromatic *act1* locus in *hht3-K9M* cells (Figure 1C). Apparently, the broad distribution of Hht3-K9M does not result in the redistribution of Clr4 across the genome, suggesting that the intrinsic affinity between Clr4 and H3K9M alone is insufficient to sequester Clr4 on chromatin, but additional mechanisms promote the sequestration of Clr4 at pericentric repeats by H3K9M.

The recent identification of CLRC as an E3 ubiquitin ligase of H3K14ub and the association of H3K14ub with heterochromatin (Oya et al., 2019; Stirpe et al., 2020) prompted us to check whether H3K14ub promotes the sequestration of Clr4 by H3K9M (Figure 2A). Interestingly, ChIP analyses show that Clr4 sequestration at pericentric repeats is abolished in *rik1Δ hht3-K9M*, *raf1Δ hht3-K9M*, and *raf2Δ hht3-K9M* cells (Figure 2B), suggesting that CLRC-mediated H3K14 ubiquitylation might indeed contribute to the sequestration of Clr4 at pericentric repeats. The complete loss of Clr4 at pericentric repeats is due to the fact that CLRC is critical for H3K9me3 and that H3K9me3 reinforces the localization of Clr4 through the interaction of H3K9me3 with the chromodomain of Clr4 (Zhang et al., 2008).

CLRC is targeted to repetitive DNA elements through the RNA interference (RNAi) pathway (Grewal and Jia, 2007) (Figure S1A). ChIP analyses show that Clr4 is not sequestered at pericentric repeats in *hht3-K9M dcr1Δ*, *hht3-K9M ago1Δ*, and *hht3-K9M chp1Δ* cells (Figure S1B). In contrast, the sequestration of Clr4 by H3K9M is independent of Swi6 (Figure S1B), which is an HP1 family protein essential for heterochromatin integrity but which functions downstream of CLRC.

To further test the requirement for H3K14ub in the sequestration of Clr4 by H3K9M, we generated an *hht3-K9MK14R* mutation, which abolishes K14 ubiquitylation selectively on H3-containing K9M. Western blot analyses show that Hht3-K9MK14R and Hht3-K9M are expressed at similar levels (Figure 2C). ChIP analyses show that Clr4 levels at pericentric *dh* repeats in *hht3-K9MK14R* cells are reduced to wild-type levels (Figure 2D).

We, then, further examined the effects of H3K9MK14R on heterochromatin function. Cells containing *hht3-K9M* are defective in the silencing of an *otr::ura4*$^+$ reporter gene inserted at the pericentric repeats, leading to the robust growth of cells on medium without uracil and little growth on medium containing 5-FOA (fluoroorotic acid) (Figure 2E). These cells also lost H3K9me3 at

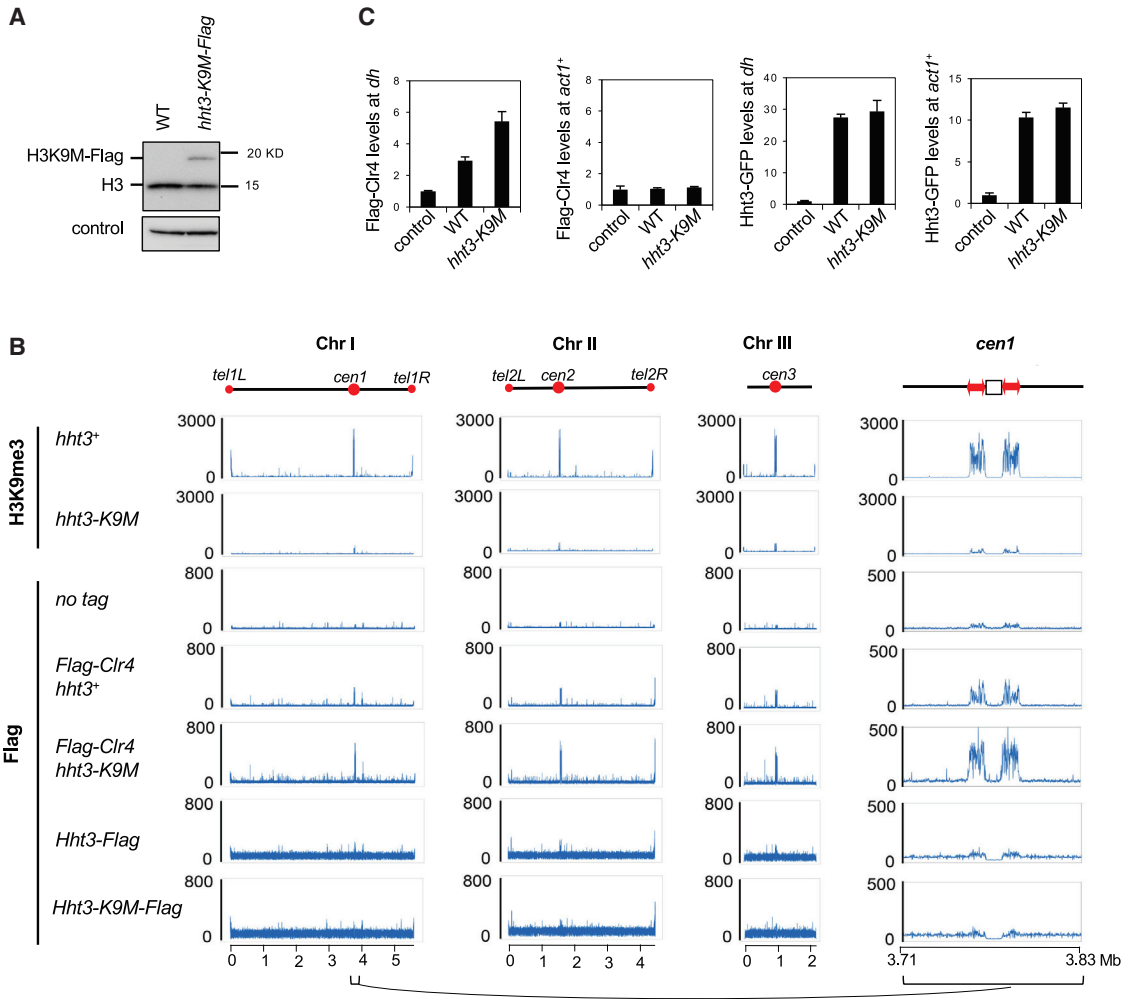

Figure 1. The selective sequestration of Clr4 at pericentric repeats by H3K9M

(A) Western blot of fission yeast cell extract with a H3 antibody. A non-specific band serves as a loading control.

(B) ChIP-seq analyses of Hht3 and Clr4 levels across the fission yeast genome. H3K9me3 data are derived from Shan et al., 2016. Diagrams of the three chromosomes are shown on top, with key positions, such as centromeres and telomeres, labeled as red circles. The region surrounding centromere I is enlarged and shown on the right. The white box indicates CENP-A containing chromatin, and the red arrows indicate pericentric heterochromatin in which H3K9me3 and Clr4 are enriched.

(C) ChIP analyses of FLAG-Clr4 and Hht3-GFP levels at pericentric *dh* repeats and *act1*$^+$. Data are presented as means ± SD of three technical replicates.

pericentric *dh* repeats, accompanied by the accumulation of *dh* RNA transcripts (Figures 2F and 2G). In *hht3-K9MK14R* cells, the silencing of *otr::ura4*$^+$ is similar to that in wild-type cells (Figure 2E). Moreover, H3K9me3 levels at pericentric *dh* repeats and *dh* RNA levels in *hht3-K9MK14R* cells are similar to those in wild-type cells (Figures 2F and 2G). Furthermore, ChIP-seq analysis shows that H3K9me3 levels are restored at all major heterochromatin domains in *hht3-K9MK14R* cells (Figure 2H). In contrast, *hht1-K14R hht3-K9M* cells are still defective in the silencing of *otr::ura4*$^+$, consistent with the fact that H3K14ub function *in cis* to regulate the activity of Clr4 on H3K9 (Oya et al., 2019; Stirpe et al., 2020) (Figures S1C and S1D).

To examine the effects of H3K14ub on the interaction between H3K9M and Clr4, we generated histone tail peptides containing ubiquitin mimics at H3K14. We synthesized biotin-tagged histone H3 tail peptides containing H3K14C and generated recombinant Ub-G76C. We then crosslinked the cysteines with 1,3 dichloroacetone (DCA) (Long et al., 2014) and purified the resulting peptides containing ubiquitin mimics at H3K14 to homogeneity (Figures 3A and S2). Peptide pull-down assays with recombinant Clr4 SET domain (residue 190–490) show that H3K9MK14ub interacts more strongly with Clr4 compared with H3K14C, H3K9MK14C, or H3K14ub in the presence of *S*-adenosyl-methionine (SAM) (Figure 3B). In addition, thermal shift assays also show that H3K9MK14ub interacts with Clr4 in the presence of SAM (Figure S3A), and Clr4 and H3K9MK14ub form a complex in the presence of SAM in a gel-filtration assay (Figures S3G and S3H). In the absence of SAM, H3K9MK14ub also results in a thermal shift of Clr4, although the shift is smaller than that observed in the presence of SAM (Figure S3B). In addition,

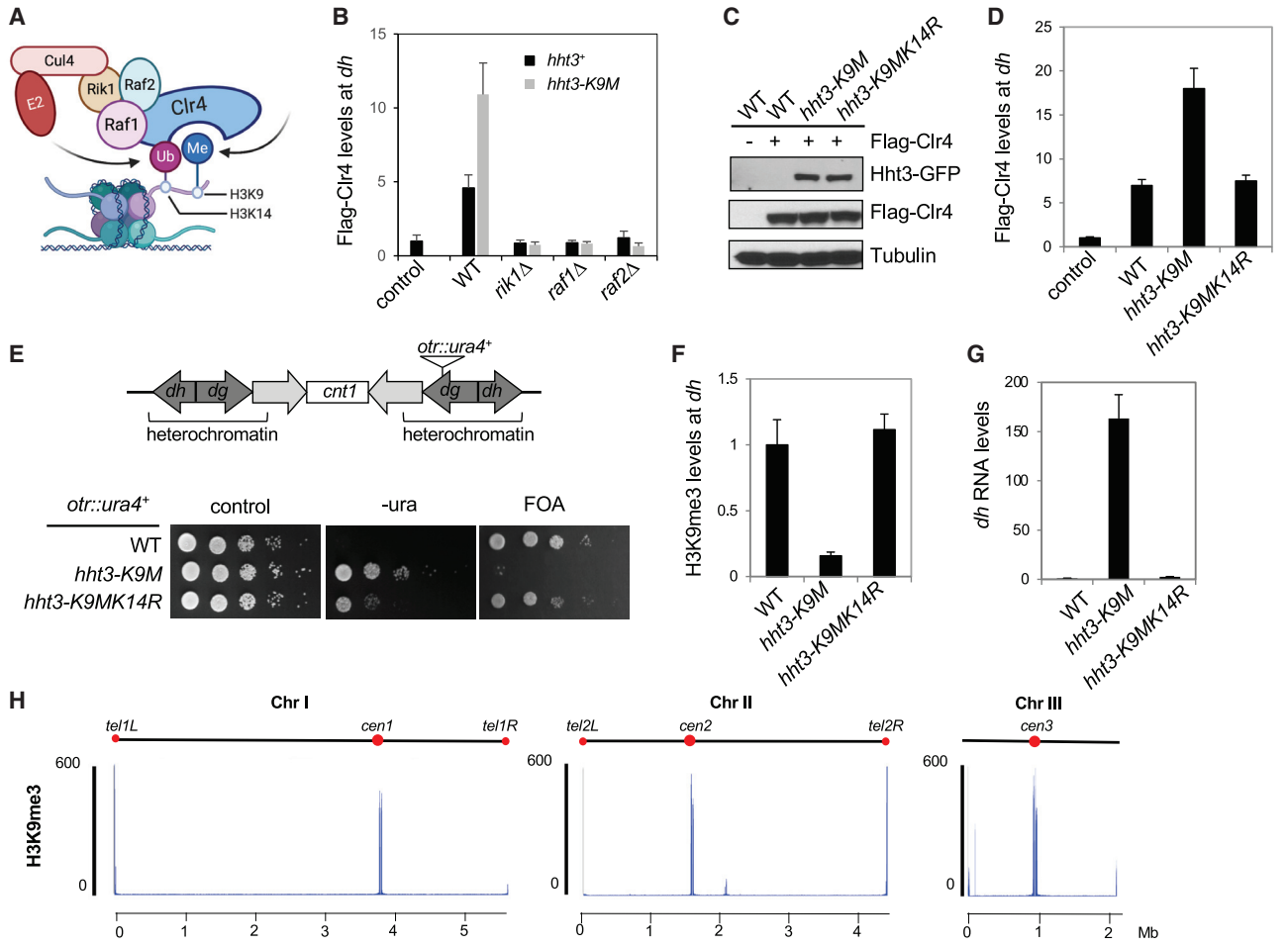

Figure 2. The requirement of CLRC-mediated H3K14ub for the sequestration of Clr4 by H3K9M at heterochromatin *in vivo*

(A) Schematic diagram of CLRC in regulating H3K14ub and H3K9 methylation.

(B and D) ChIP analysis of FLAG-Clr4 levels at pericentric *dh* repeats, normalized to *act1*$^+$. Data are presented as means ± SD of three technical replicates.

(C) Western blot analysis of Hht3 and Clr4 levels. Tubulin is used as loading control.

(E) Top, schematic diagram of the *otr::ura4*$^+$ reporter. Bottom, serial dilution analysis of indicated strains to measure the expression of *otr::ura4*$^+$.

(F) ChIP analysis of H3K9me3 levels at pericentric *dh* repeats, normalized to *act1*$^+$. Data are presented as means ± SD of three technical replicates.

(G) qRT-PCR analysis of pericentric *dh* repeats, normalized to *act1*$^+$. Data are presented as mean ± SD of 3 technical replicates.

(H) ChIP-seq analyses of H3K9me3 levels across the fission yeast genome in cells expressing H3K9MK14R.

See also Figure S1.

H3K14ub results in an intermediate thermal shift of Clr4 in the absence of SAM, which is not observed in the presence of SAM. This is likely because the combination of Clr4, H3K14ub, and SAM results in H3K9 methylation reaction, which might lead to the dissociation of the complex. We also noticed that the addition of SAM alone, without peptide, results in greater thermal stability of Clr4, which might explain why SAM is important for binding (Figure S3C).

We further used bio-layer interferometry (BLI) to quantify the interactions (Figure 3C). In the presence of SAM, the equilibrium dissociation constant (K_D) of the Clr4-SET interaction with H3K9MK14C, H3K14ub, and H3K9MK14ub is 1.42 μM, 0.61 μM, and 0.34 μM, respectively, whereas the K_D of the Clr4 interaction with H3K14C is below detection. Comparing H3K9MK14C with H3K9MK14ub, k_{on} increases from 50,770 $M^{-1}s^{-1}$ to 118,400 $M^{-1}s^{-1}$, whereas k_{off} decreases from 0.0723 s^{-1} to 0.0405 s^{-1}, resulting in $t_{1/2}$ changes from 9.6 to 17.1 s. These results suggest that the presence of H3K14ub increases the association but decreases the dissociation of Clr4 with H3K9M. Comparing H3K14ub and H3K9MK14ub, the association rate k_{on} decreases from 228,900 $M^{-1}s^{-1}$ to 118,400 $M^{-1}s^{-1}$, whereas the dissociate rate k_{off} decreases from 0.1410 s^{-1} to 0.0405 s^{-1}, resulting in $t_{1/2}$ changes from 4.9 to 17.1 s. These results suggest that, in the presence of H3K14ub, it is more difficult for Clr4 to get on to H3K9M than on to H3K9. Once Clr4 is bound to H3K9M, it is also more difficult for Clr4 to get off.

In the absence of SAM, Clr4-SET interaction with H3K14ub is mildly reduced (K_D increased from 0.61 μM to 1.02 μM), but the interaction between Clr4-SET and H3K9MK14ub is reduced more dramatically (K_D increased from 0.34 μM to 2.44 μM)

CellPress
OPEN ACCESS

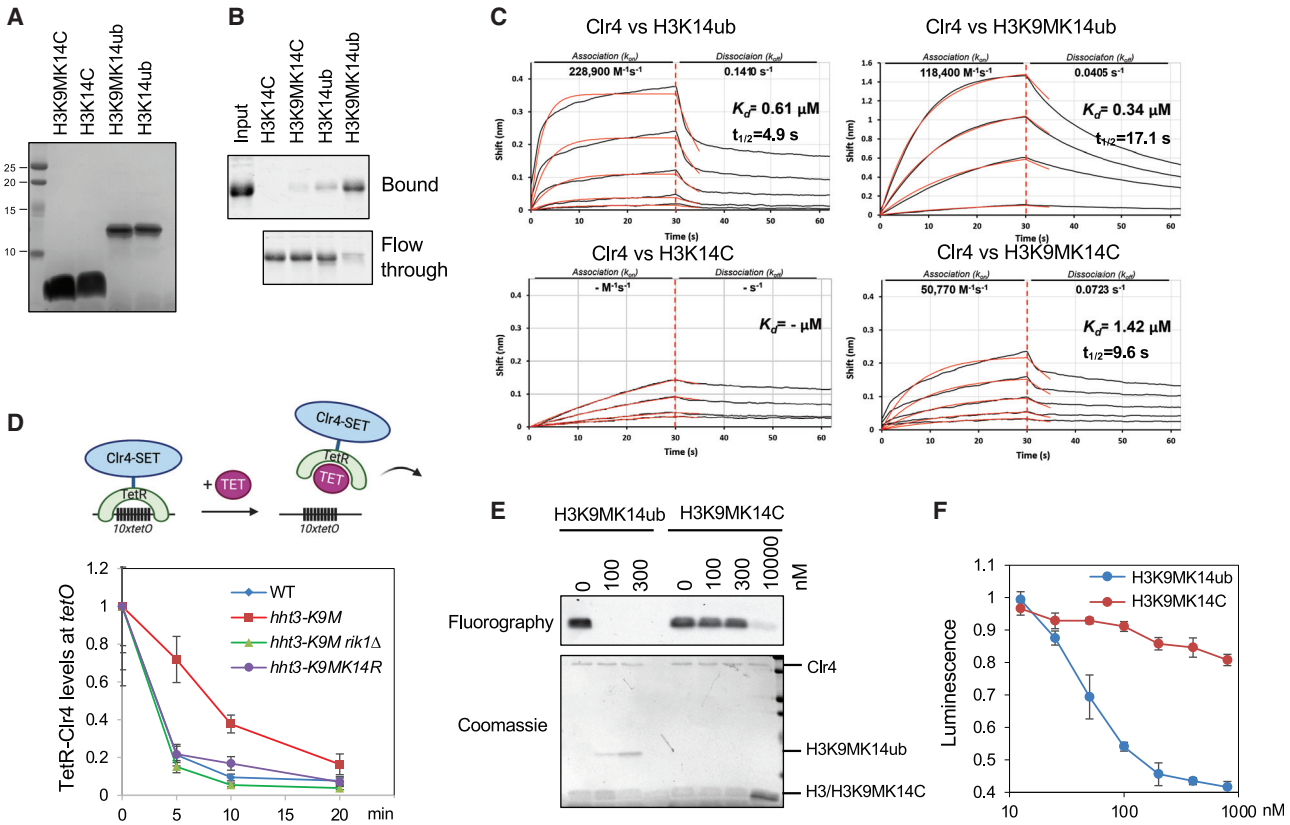

Figure 3. H3K14ub enhances the interaction between Clr4 and H3K9M

(A) SDS-PAGE analysis of peptides used. The gel is stained with Coomassie blue.

(B) SDS-PAGE analysis of Clr4-SET bound to different peptides as well as the corresponding flow-through fractions. The gel is stained with Coomassie blue.

(C) BLI analyses of the interaction of Clr4-SET with different histone H3-tail peptides.

(D) ChIP analysis of FLAG-TetR-Clr4-SET levels at *tetO* at different time points after the addition of tetracycline, normalized to *act1*$^{+}$. Data are presented as means ± SD of three technical replicates.

(E) *In vitro* histone methyltransferase assays using Clr4-SET, ^{3}H-SAM, H3-tail peptide, and the indicated amounts of H3K9M or H3K9MK14ub peptides. The reaction product is resolved by SDS-PAGE, stained with Coomassie blue (bottom), and processed for fluorography (top).

(F) *In vitro* histone methyltransferase assays using Clr4-SET, SAM, H3-tail peptide, and varying amounts of H3K9M or H3K9MK14ub peptides. The concentration of methylation reaction product *S*-adenosyl-homocysteine (SAH) was measured by luminescence levels (RLUs, relative light units) after being processed with the MTase Glo assay kit. Data are presented as means ± SD of two technical replicates.

See also Figures S2–S4.

(Figure S4A). SAM mainly affects the k_{on} of Clr4-SET and H3K9MK14ub interaction (1189,400 $M^{-1}s^{-1}$ and 23,550 $M^{-1}s^{-1}$ in the presence and absence of SAM, respectively), suggesting that the presence of SAM helps Clr4 recognize the H3K9M mutation.

To examine whether the presence of H3K9M slows down the turnover of Clr4 on chromatin *in vivo*, we used a strain in which Clr4 is targeted to 10 copies of the *tetO* binding sites through a TetR-Clr4 fusion protein (Figure 3D), which results in the formation of a large, ectopic heterochromatin domain. This ectopic heterochromatin also depends on every component of CLRC (Raguna-than et al., 2015). ChIP analyses show that the addition of tetracycline results in the quick release of Clr4 from chromatin, with most TetR-Clr4 released from the *tetO* sites within 5 min of tetracycline addition (Figure 3D). In *hht3-K9M* cells, we observed a delay in the release of TetR-Clr4 (Figure 3D), suggesting that the presence of H3K9M-containing nucleosomes, indeed, slows down the turnover of Clr4 on chromatin. In both *hht3-K9M rik1Δ* and *hht3-K9MK14R* cells, the release of TetR-Clr4 is similar to the rate in wild-type cells, suggesting that H3K14ub contributes to the slow turnover of Clr4 on chromatin in *hht3-K9M* cells (Figure 3D).

We also examined whether the presence of H3K14ub enhances the inhibitory effects of H3K9M on Clr4 enzymatic activity *in vitro*. Using a histone methyltransferase assay with recombinant Clr4 SET domain (190–490), ^{3}H-labeled SAM as the methyl donor, and histone H3 tail peptide as the substrate, we found that H3K9MK14ub is a more-potent inhibitor compared with H3K9M (Figure 3E). A non-radioactive methyltransferase assay that measures the production of *S*-adenosyl-homocysteine also confirmed that conclusion (Figure 3F).

Hydrogen/deuterium exchange coupled to mass spectrometry analysis shows that the interaction between Clr4 and H3K14ub is

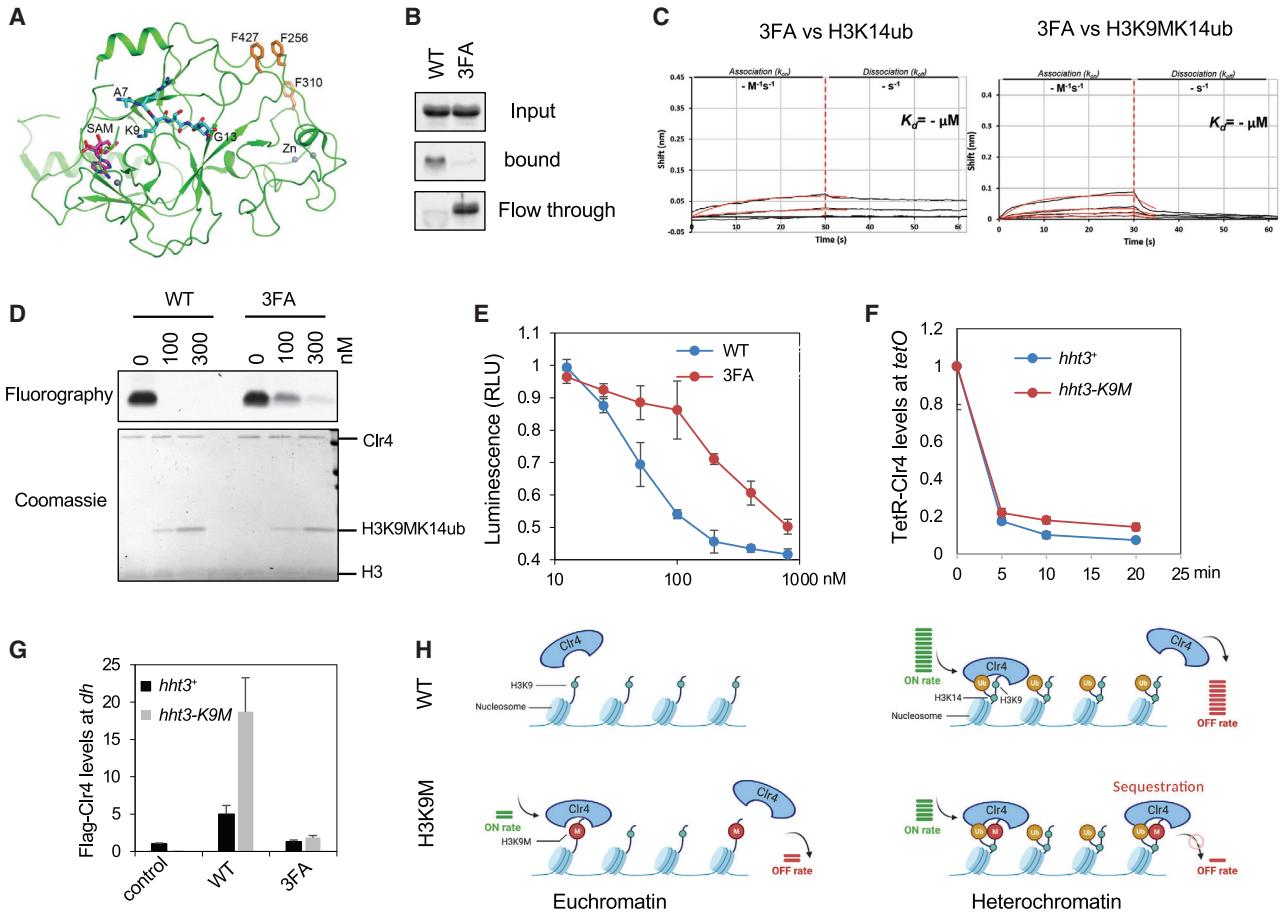

Figure 4. The 3FA mutation comprised the interaction between Clr4 and H3K9MK14ub and relieved the sequestration of Clr4 by H3K9M *in vivo*

(A) Structure representation of Clr4 based on PDB: 6BP4 (Iglesias et al., 2018). The three residues mutated in 3FA (F256, F310, and F427), SAM, and the H3 peptide are presented as stick models. The H3 peptide is modeled based on the Dim-5-H3 complex structure (PDB: 1PEG) (Zhang et al., 2003).

(B) SDS-PAGE analysis of Clr4 or Clr4-3FA bound to H3K9MK14ub as well as the corresponding flow-through fraction. The gel is stained with Coomassie blue.

(C) BLI analysis of the interaction of Clr4-3FA H3K9MK14ub peptide.

(D) *In vitro* histone methyltransferase assays were performed with Clr4-SET, ^{3}H-SAM, H3 tail peptide, and indicated amounts of H3K9M or H3K9MK14ub peptides.

(E) *In vitro* histone methyltransferase assays were performed with Clr4-SET, SAM, H3 peptide, and varying amounts of H3K9MK14ub peptides. The production of SAH was measured by luminescence levels after being processed with MTase Glo assay kit. Data are presented as means ± SD of two technical replicates.

(F) ChIP analysis of FLAG-TetR-Clr4 levels at pericentric *tetO*, normalized to *act1*$^{+}$. Data are presented as means ± SD of three technical replicates.

(G) ChIP analysis of FLAG-Clr4 levels at pericentric *dh* repeats, normalized to *act1*$^{+}$. Data are presented as means ± SD of three technical replicates.

(H) A model for the selective sequestration of Clr4 by H3K9M at pericentric repeats.

See also Figures S3 and S4.

mediated by a hydrophobic surface of Clr4 that includes residues F256, F310, and F427 (Stirpe et al., 2020) (Figure 4A). We generated a recombinant Clr4 SET domain containing the F256A, F310A, and F427A mutations (3FA). That mutation strongly reduced the interaction between Clr4 and H3K14ub and has little effect on the structure of Clr4 (Stirpe et al., 2020). Peptide pull-down assays, thermal-shift assays, and BLI, all demonstrate that the 3FA mutation strongly reduces the interaction between Clr4 and H3K9MK14ub, either in the presence or in the absence of SAM (Figures 4B, 4C, S3D–S3F, S4B, and S4C). In addition, *in vitro* histone methyltransferase assays show that the 3FA mutant is less sensitive to H3K9MK14ub compared with that of wild-type Clr4 (Figures 4D and 4E), suggesting that the interaction of Clr4 with H3K14ub is critical for the inhibitory effects of H3K9M. To test the effects of 3FA on the sequestration of Clr4 by H3K9M *in vivo*, we generated a strain expressing TetR-Clr4-3FA. ChIP analyses show that TetR-Clr4-3FA is quickly released from the *tetO* locus in both wild-type and *hht3-K9M* cells (Figure 4F), suggesting that Clr4-3FA is not sequestered by H3K9M. We also used a strain expressing Clr4-3FA at its endogenous chromosomal locus. In *hht3-K9M* cells, the sequestration of Clr4-3FA mutant at pericentric repeats is abolished compared with that of wild-type Clr4 (Figure 4G). Again, the complete loss of Clr4-3FA at pericentric repeats is likely due to the requirement of

H3K9me3 for the stable association of Clr4 at those regions, given the effect of Clr4-3FA on H3K9me3 *in vivo* (Stirpe et al., 2020). These results demonstrate that reducing the interaction between Clr4 and H3K9MK14ub decreases the inhibitory effects of H3K9M on Clr4 enzymatic activity and compromises the ability of H3K9M to sequester Clr4 on chromatin.

Altogether, our results suggest that the affinity between Clr4 and H3K9M is low, thus H3K9M by itself is insufficient to sequester Clr4 on chromatin. At heterochromatin regions, CLRC catalyzes the H3K14ub, which increases the affinity of Clr4 to the H3 tail and enhances its enzymatic activity. H3K9M synergizes with H3K14ub to interact with Clr4, leading to the selective sequestration of Clr4 at heterochromatin. In euchromatin regions, the absence of H3K14ub coupled with the lower k_{on} of Clr4 to H3K9M prevents Clr4 sequestration by H3K9M due to the reduced ability of Clr4 to load on to H3K9M-containing nucleosomes (Figure 4H). In addition, our BLI data also highlights the importance of protein-protein interaction kinetic properties, which can be masked by affinity measurements, in regulating biological processes.

One of the key discrepancies regarding the methyltransferase sequestration model is in the case of H3.3K27M, in which most foci with high levels of H3.3K27M show little enrichment of the H3K27 methyltransferase PRC2 (Piunti et al., 2017). Although the reason for such a discrepancy is complex (Fang et al., 2018; Sarthy et al., 2020; Stafford et al., 2018), we speculate that additional mechanisms at defined genomic locations might change the kinetic properties of PRC2-H3.3K27M interactions, leading to sequestration of PRC2 at selective loci. Indeed, in H3.3K27M-expressing cells, PRC2 is sequestered at poised enhancers (Fang et al., 2018), and the H3.3K27M-PRC2 interactions can be modulated by the presence of H3K27me3 (Diehl et al., 2019; Stafford et al., 2018). In addition, although H3K27M enhances the interaction between PRC2 and the H3 tail peptide, it has a minor role in the interaction between PRC2 and the nucleosome (Wang et al., 2017), which is consistent with the idea that H3K27M alone is insufficient to sequester PRC2. Interestingly, structural analysis shows that the association of PRC2 with nucleosome is regulated by JARID2-AEBP2 and H2AK119ub (Kasinath et al., 2021). It would be interesting to examine whether H2AK119ub promotes the sequestration of PRC2 by H3K27M, similar to the effects of H3K14ub on the sequestration of Clr4 by H3K9M.

Similar to CLRC in fission yeast, the *Neurospora crassa* H3K9 methyltransferase Dim-5 and mammalian H3K9 methyltransferase SUV39H1 also associate with CUL4-based E3 ubiquitin ligase complexes (Lewis et al., 2010; Yang et al., 2015). In both organisms, CUL4, its adaptor protein DDB1, and the associated DCAFs (DDB1 and CUL4-associated factors) are also required for H3K9 methylation (Higa et al., 2006; Lewis et al., 2010; Xu et al., 2010; Zhao et al., 2010). Although mammalian CUL4-DDB1 complex ubiquitylates histone H3 *in vitro* (Wang et al., 2006), it remains to be determined whether CUL4-DDB1 ubiquitylates H3K14. H3K14ub stimulates the activity of mammalian H3K9 methyltransferase SUV39H1 *in vitro* (Stirpe et al., 2020), suggesting that the cross-talk between H3K14ub and H3K9me3 might be conserved. H3K14ub is detected by mass spectrometry analysis of mammalian histones (Kim et al., 2011). Therefore, it would be interesting to further examine whether the crosstalk between H3K14ub and H3K9me is conserved in higher organisms *in vivo* and how H3K14ub is regulated during biological processes.

STAR★METHODS

Detailed methods are provided in the online version of this paper and include the following:

- KEY RESOURCES TABLE
- RESOURCE AVAILABILITY
  - Lead contact
  - Materials availability
  - Data and code availability
- EXPERIMENTAL MODEL AND SUBJECT DETAILS
- METHOD DETAILS
  - Serial dilution analyses
  - Chromatin immunoprecipitation (ChIP) analyses
  - ChIP-seq
  - ChIP-seq of H3K9me3 in hht3-K9MK14R cells
  - RNA analyses
  - Western blot analyses
  - Generation of peptides containing H3K14ub mimics
  - Protein expression and purification
  - Peptide binding assays
  - Thermal shift assay
  - Biolayer interferometry
  - *In vitro* histone methyltransferase assays
- QUANTIFICATION AND STATISTICAL ANALYSIS

SUPPLEMENTAL INFORMATION

Supplemental information can be found online at https://doi.org/10.1016/j.celrep.2021.109137.

ACKNOWLEDGMENTS

We thank Danesh Moazed, Kaushik Ragunathan, and Tingting Yao for strains and plasmids; Jia Wei for help with thermal shift assay; and members of the Jia laboratory for discussions and comments on the manuscript. This work was supported by NIH grants R35GM126910 to S.J., R35GM118093 to L.T., and R01GM098943 to F.Q., and an American Cancer Society research scholar grant RSG-16-041-01-DMC to F.Q.

AUTHOR CONTRIBUTIONS

C.-M.S. and S.J. conceived the project; C.-M.S., S.J., F.Q., and L.T. designed experiments; and C.-M.S., J.K.-K., J.W., K.B., Y.S., H.C., and S.J. performed experiments. J.-X.Y. performed the ChIP-seq data analysis, A.S. and T.S. provided the *clr4-3FA* yeast strain and shared information before publication, and Z.Z. and C.L. provided antibodies. S.J., F.Q., L.T., P.L.N., and G.L. supervised the research. S.J wrote the paper with input from all authors.

DECLARATION OF INTERESTS

The authors declare no competing interest.

Received: November 4, 2020
Revised: March 5, 2021
Accepted: April 24, 2021
Published: May 18, 2021

REFERENCES

Behjati, S., Tarpey, P.S., Presneau, N., Scheipl, S., Pillay, N., Van Loo, P., Wedge, D.C., Cooke, S.L., Gundem, G., Davies, H., et al. (2013). Distinct H3F3A and H3F3B driver mutations define chondroblastoma and giant cell tumor of bone. Nat. Genet. *45*, 1479–1482.

Bender, S., Tang, Y., Lindroth, A.M., Hovestadt, V., Jones, D.T., Kool, M., Zapatka, M., Northcott, P.A., Sturm, D., Wang, W., et al. (2013). Reduced H3K27me3 and DNA hypomethylation are major drivers of gene expression in K27M mutant pediatric high-grade gliomas. Cancer Cell *24*, 660–672.

Brumbaugh, J., Kim, I.S., Ji, F., Huebner, A.J., Di Stefano, B., Schwarz, B.A., Charlton, J., Coffey, A., Choi, J., Walsh, R.M., et al. (2019). Inducible histone K-to-M mutations are dynamic tools to probe the physiological role of site-specific histone methylation in vitro and in vivo. Nat. Cell Biol. *21*, 1449–1461.

Chan, K.M., Fang, D., Gan, H., Hashizume, R., Yu, C., Schroeder, M., Gupta, N., Mueller, S., James, C.D., Jenkins, R., et al. (2013a). The histone H3.3K27M mutation in pediatric glioma reprograms H3K27 methylation and gene expression. Genes Dev. *27*, 985–990.

Chan, K.M., Han, J., Fang, D., Gan, H., and Zhang, Z. (2013b). A lesson learned from the H3.3K27M mutation found in pediatric glioma: a new approach to the study of the function of histone modifications in vivo? Cell Cycle *12*, 2546–2552.

Diehl, K.L., Ge, E.J., Weinberg, D.N., Jani, K.S., Allis, C.D., and Muir, T.W. (2019). PRC2 engages a bivalent H3K27M-H3K27me3 dinucleosome inhibitor. Proc. Natl. Acad. Sci. USA *116*, 22152–22157.

Fang, D., Gan, H., Lee, J.H., Han, J., Wang, Z., Riester, S.M., Jin, L., Chen, J., Zhou, H., Wang, J., et al. (2016). The histone H3.3K36M mutation reprograms the epigenome of chondroblastomas. Science *352*, 1344–1348.

Fang, D., Gan, H., Cheng, L., Lee, J.H., Zhou, H., Sarkaria, J.N., Daniels, D.J., and Zhang, Z. (2018). H3.3K27M mutant proteins reprogram epigenome by sequestering the PRC2 complex to poised enhancers. eLife *7*, e36696.

Funato, K., Major, T., Lewis, P.W., Allis, C.D., and Tabar, V. (2014). Use of human embryonic stem cells to model pediatric gliomas with H3.3K27M histone mutation. Science *346*, 1529–1533.

Grewal, S.I., and Jia, S. (2007). Heterochromatin revisited. Nat. Rev. Genet. *8*, 35–46.

Herz, H.M., Morgan, M., Gao, X., Jackson, J., Rickels, R., Swanson, S.K., Florens, L., Washburn, M.P., Eissenberg, J.C., and Shilatifard, A. (2014). Histone H3 lysine-to-methionine mutants as a paradigm to study chromatin signaling. Science *345*, 1065–1070.

Higa, L.A., Wu, M., Ye, T., Kobayashi, R., Sun, H., and Zhang, H. (2006). CUL4-DDB1 ubiquitin ligase interacts with multiple WD40-repeat proteins and regulates histone methylation. Nat. Cell Biol. *8*, 1277–1283.

Hong, E.J., Villén, J., Gerace, E.L., Gygi, S.P., and Moazed, D. (2005). A cullin E3 ubiquitin ligase complex associates with Rik1 and the Clr4 histone H3-K9 methyltransferase and is required for RNAi-mediated heterochromatin formation. RNA Biol. *2*, 106–111.

Horn, P.J., Bastie, J.N., and Peterson, C.L. (2005). A Rik1-associated, cullin-dependent E3 ubiquitin ligase is essential for heterochromatin formation. Genes Dev. *19*, 1705–1714.

Iglesias, N., Currie, M.A., Jih, G., Paulo, J.A., Siuti, N., Kalocsay, M., Gygi, S.P., and Moazed, D. (2018). Automethylation-induced conformational switch in Clr4 (Suv39h) maintains epigenetic stability. Nature *560*, 504–508.

Jayaram, H., Hoelper, D., Jain, S.U., Cantone, N., Lundgren, S.M., Poy, F., Allis, C.D., Cummings, R., Bellon, S., and Lewis, P.W. (2016). S-adenosyl methionine is necessary for inhibition of the methyltransferase G9a by the lysine 9 to methionine mutation on histone H3. Proc. Natl. Acad. Sci. USA *113*, 6182–6187.

Jia, S., Kobayashi, R., and Grewal, S.I. (2005). Ubiquitin ligase component Cul4 associates with Clr4 histone methyltransferase to assemble heterochromatin. Nat. Cell Biol. *7*, 1007–1013.

Justin, N., Zhang, Y., Tarricone, C., Martin, S.R., Chen, S., Underwood, E., De Marco, V., Haire, L.F., Walker, P.A., Reinberg, D., et al. (2016). Structural basis of oncogenic histone H3K27M inhibition of human polycomb repressive complex 2. Nat. Commun. *7*, 11316.

Kasinath, V., Beck, C., Sauer, P., Poepsel, S., Kosmatka, J., Faini, M., Toso, D., Aebersold, R., and Nogales, E. (2021). JARID2 and AEBP2 regulate PRC2 in the presence of H2AK119ub1 and other histone modifications. Science *371*, eabc3393.

Kim, W., Bennett, E.J., Huttlin, E.L., Guo, A., Li, J., Possemato, A., Sowa, M.E., Rad, R., Rush, J., Comb, M.J., et al. (2011). Systematic and quantitative assessment of the ubiquitin-modified proteome. Mol. Cell *44*, 325–340.

Langmead, B., and Salzberg, S.L. (2012). Fast gapped-read alignment with Bowtie 2. Nat. Methods *9*, 357–359.

Lewis, Z.A., Adhvaryu, K.K., Honda, S., Shiver, A.L., Knip, M., Sack, R., and Selker, E.U. (2010). DNA methylation and normal chromosome behavior in Neurospora depend on five components of a histone methyltransferase complex, DCDC. PLoS Genet. *6*, e1001196.

Lewis, P.W., Müller, M.M., Koletsky, M.S., Cordero, F., Lin, S., Banaszynski, L.A., Garcia, B.A., Muir, T.W., Becher, O.J., and Allis, C.D. (2013). Inhibition of PRC2 activity by a gain-of-function H3 mutation found in pediatric glioblastoma. Science *340*, 857–861.

Lock, A., Rutherford, K., Harris, M.A., Hayles, J., Oliver, S.G., Bähler, J., and Wood, V. (2019). PomBase 2018: user-driven reimplementation of the fission yeast database provides rapid and intuitive access to diverse, interconnected information. Nucleic Acids Res. *47* (*D1*), D821–D827.

Long, L., Furgason, M., and Yao, T. (2014). Generation of nonhydrolyzable ubiquitin-histone mimics. Methods *70*, 134–138.

Lu, C., Jain, S.U., Hoelper, D., Bechet, D., Molden, R.C., Ran, L., Murphy, D., Venneti, S., Hameed, M., Pawel, B.R., et al. (2016). Histone H3K36 mutations promote sarcomagenesis through altered histone methylation landscape. Science *352*, 844–849.

Mohammad, F., Weissmann, S., Leblanc, B., Pandey, D.P., Højfeldt, J.W., Comet, I., Zheng, C., Johansen, J.V., Rapin, N., Porse, B.T., et al. (2017). EZH2 is a potential therapeutic target for H3K27M-mutant pediatric gliomas. Nat. Med. *23*, 483–492.

Oya, E., Nakagawa, R., Yoshimura, Y., Tanaka, M., Nishibuchi, G., Machida, S., Shirai, A., Ekwall, K., Kurumizaka, H., Tagami, H., and Nakayama, J.I. (2019). H3K14 ubiquitylation promotes H3K9 methylation for heterochromatin assembly. EMBO Rep. *20*, e48111.

Papillon-Cavanagh, S., Lu, C., Gayden, T., Mikael, L.G., Bechet, D., Karamboulas, C., Ailles, L., Karamchandani, J., Marchione, D.M., Garcia, B.A., et al. (2017). Impaired H3K36 methylation defines a subset of head and neck squamous cell carcinomas. Nat. Genet. *49*, 180–185.

Piunti, A., Hashizume, R., Morgan, M.A., Bartom, E.T., Horbinski, C.M., Marshall, S.A., Rendleman, E.J., Ma, Q., Takahashi, Y.H., Woodfin, A.R., et al. (2017). Therapeutic targeting of polycomb and BET bromodomain proteins in diffuse intrinsic pontine gliomas. Nat. Med. *23*, 493–500.

Ragunathan, K., Jih, G., and Moazed, D. (2015). Epigenetics. Epigenetic inheritance uncoupled from sequence-specific recruitment. Science *348*, 1258699.

Ramírez, F., Ryan, D.P., Grüning, B., Bhardwaj, V., Kilpert, F., Richter, A.S., Heyne, S., Dündar, F., and Manke, T. (2016). deepTools2: a next generation web server for deep-sequencing data analysis. Nucleic Acids Res. *44* (*W1*), W160–W165.

Robinson, J.T., Thorvaldsdóttir, H., Winckler, W., Guttman, M., Lander, E.S., Getz, G., and Mesirov, J.P. (2011). Integrative genomics viewer. Nat. Biotechnol. *29*, 24–26.

Sarthy, J.F., Meers, M.P., Janssens, D.H., Henikoff, J.G., Feldman, H., Paddison, P.J., Lockwood, C.M., Vitanza, N.A., Olson, J.M., Ahmad, K., and Henikoff, S. (2020). Histone deposition pathways determine the chromatin landscapes of H3.1 and H3.3 K27M oncohistones. eLife *9*, e61090.

Schwartzentruber, J., Korshunov, A., Liu, X.Y., Jones, D.T., Pfaff, E., Jacob, K., Sturm, D., Fontebasso, A.M., Quang, D.A., Tönjes, M., et al. (2012). Driver mutations in histone H3.3 and chromatin remodelling genes in paediatric glioblastoma. Nature *482*, 226–231.

Shan, C.M., Wang, J., Xu, K., Chen, H., Yue, J.X., Andrews, S., Moresco, J.J., Yates, J.R., Nagy, P.L., Tong, L., and Jia, S. (2016). A histone H3K9M mutation traps histone methyltransferase Clr4 to prevent heterochromatin spreading. eLife *5*, e17903.

Stafford, J.M., Lee, C.H., Voigt, P., Descostes, N., Saldaña-Meyer, R., Yu, J.R., Leroy, G., Oksuz, O., Chapman, J.R., Suarez, F., et al. (2018). Multiple modes of PRC2 inhibition elicit global chromatin alterations in H3K27M pediatric glioma. Sci. Adv. *4*, eaau5935.

Stirpe, A., Guidotti, N., Northall, S., Kilic, S., Hainard, A., Vadas, O., Fierz, B., and Schalch, T. (2020). SUV39 SET domains mediate crosstalk of heterochromatic histone marks. bioRxiv, 2020.0630.177071.

Sturm, D., Witt, H., Hovestadt, V., Khuong-Quang, D.A., Jones, D.T., Konermann, C., Pfaff, E., Tönjes, M., Sill, M., Bender, S., et al. (2012). Hotspot mutations in H3F3A and IDH1 define distinct epigenetic and biological subgroups of glioblastoma. Cancer Cell *22*, 425–437.

Wang, H., Zhai, L., Xu, J., Joo, H.Y., Jackson, S., Erdjument-Bromage, H., Tempst, P., Xiong, Y., and Zhang, Y. (2006). Histone H3 and H4 ubiquitylation by the CUL4-DDB-ROC1 ubiquitin ligase facilitates cellular response to DNA damage. Mol. Cell *22*, 383–394.

Wang, X., Paucek, R.D., Gooding, A.R., Brown, Z.Z., Ge, E.J., Muir, T.W., and Cech, T.R. (2017). Molecular analysis of PRC2 recruitment to DNA in chromatin and its inhibition by RNA. Nat. Struct. Mol. Biol. *24*, 1028–1038.

Wu, G., Broniscer, A., McEachron, T.A., Lu, C., Paugh, B.S., Becksfort, J., Qu, C., Ding, L., Huether, R., Parker, M., et al.; St. Jude Children's Research Hospital–Washington University Pediatric Cancer Genome Project (2012). Somatic histone H3 alterations in pediatric diffuse intrinsic pontine gliomas and non-brainstem glioblastomas. Nat. Genet. *44*, 251–253.

Xu, H., Wang, J., Hu, Q., Quan, Y., Chen, H., Cao, Y., Li, C., Wang, Y., and He, Q. (2010). DCAF26, an adaptor protein of Cul4-based E3, is essential for DNA methylation in *Neurospora crassa*. PLoS Genet. *6*, e1001132.

Yang, Y., Liu, R., Qiu, R., Zheng, Y., Huang, W., Hu, H., Ji, Q., He, H., Shang, Y., Gong, Y., and Wang, Y. (2015). CRL4B promotes tumorigenesis by coordinating with SUV39H1/HP1/DNMT3A in DNA methylation-based epigenetic silencing. Oncogene *34*, 104–118.

Zhang, X., Yang, Z., Khan, S.I., Horton, J.R., Tamaru, H., Selker, E.U., and Cheng, X. (2003). Structural basis for the product specificity of histone lysine methyltransferases. Mol. Cell *12*, 177–185.

Zhang, K., Mosch, K., Fischle, W., and Grewal, S.I. (2008). Roles of the Clr4 methyltransferase complex in nucleation, spreading and maintenance of heterochromatin. Nat. Struct. Mol. Biol. *15*, 381–388.

Zhang, Y., Shan, C.M., Wang, J., Bao, K., Tong, L., and Jia, S. (2017). Molecular basis for the role of oncogenic histone mutations in modulating H3K36 methylation. Sci. Rep. *7*, 43906.

Zhao, Y., Shen, Y., Yang, S., Wang, J., Hu, Q., Wang, Y., and He, Q. (2010). Ubiquitin ligase components Cullin4 and DDB1 are essential for DNA methylation in *Neurospora crassa*. J. Biol. Chem. *285*, 4355–4365.

STAR★METHODS

KEY RESOURCES TABLE

REAGENT or RESOURCE	SOURCE	IDENTIFIER
Antibodies		
Anti-flag M2 affinity gel	Sigma	Cat# A2220; RRID:AB_10063035
Anti-Tublin	Keith Gull lab	N/A
Mouse Anti-Green Fluorescent Protein (GFP) Monoclonal Antibody	Covance	Cat# MMS-118P-500; RRID:AB_291290
Mouse monoclonal anti-FLAG	Sigma	Cat#F3165; RRID:AB_259529
Chemicals, peptides, and recombinant proteins		
2,2′-Dithiobis(5-nitropyridine)(DCA)	Sigma-Aldrich	Cat#158194
5-Fluoroorotic Acid Monohydrate (FOA, 5-FOA)	US Biological	Cat#F5050
D-biotin	Sigma-Aldrich	Cat#2031
EN3HANCE	Perkin Elmer	Cat#6NE9701
Formaldehyde, 37% solution	Sigma	Cat#F8775
H3K14C-biotin, H3K9MK14C-biotin peptides	Biomatik	Custom
Hygromycin B	Gold Biotechnology	Cat#H-270-10
Isopropyl-1-thio-D-galactopyranoside (IPTG)	Fisher Bioreagents	Cat#BP1755
MNase	Thermo Fisher Scientific	Cat#88216
Phenol-chloroform-isoamyl alcohol mixture	Sigma	Cat#77617
Proteinase K	Invitrogen	Cat#10005393
RNAase A	Thermo Fisher Scientific	Cat#EN0531
S-Adenosyl methionine (SAM)	Sigma	Cat#A7007
Sodium deoxycholate	Sigma-Aldrich	Cat#D6750
SYPRO orange	Invitrogen	Cat#S6650
Tris (2-carboxyethyl) phosphine hydrochloride (TCEP)	Aldrich	Cat#C4706
^{3}H-SAM	Perkin Elmer	Cat#NET155H250UC
Critical commercial assays		
Power SYBR Green RNA-to-CT one-step Kit	Thermo Fisher Scientific	4389986
MasterPure yeast RNA purification kit	Epicenter	MPY03100
Maxima SYBR Green qPCR Master Mix	ThermoFisher Scientific	K0223
Avidin agarose column	Thermo Scientific	20228
Talon metal affinity resin	TakaraBio USA	635501
MTase-Glo Methyltransferase Assay kit	Promega	V7601
Deposited data		
Sequencing Data	This paper	GSE159192
Experimental models: Organisms/strains		
S. pombe, see Table S1	Jia Lab Strains	N/A
Oligonucleotides		
Primer: qPCR at *act1*+, Forward: GGTGGTATGAAGCCGTTGAT	This paper	N/A
Primer: qPCR at *act1*+, Reverse: AGTGCTAACGCTGTGTGTGG	This paper	N/A

(*Continued on next page*)

Continued

REAGENT or RESOURCE	SOURCE	IDENTIFIER
Primer: qPCR at *dh,* Forward: AATGACAAAGGTGCCGAATC	This paper	N/A
Primer: qPCR at *dh*, Reverse: CGTTGAATGTTGTTGCTTTCA	This paper	N/A
Primer: qPCR at *tetO,* Forward: AATGACAAAGGTGCCGAATC	This paper	N/A
Primer: qPCR at *tetO,* Reverse: CTTCCCTGCCTATCGACAAC	This paper	N/A
Software and algorithms		
Picard tools v2.0.1	Broad Institute, MIT	https://broadinstitute.github.io/picard/
Trimmomatic v0.35	Max Planck Institute of Molecular Plant Physiology	http://www.usadellab.org/cms/?page=trimmomatic
ForteBio Data analysis	ForteBio	v10.0.1.6
Samtools v1.2	Wellcome Trust Sanger Institute	http://samtools.sourceforge.net/
GATK v3.5	Broad Institute, MIT	https://github.com/broadinstitute/gatk/releases
Bwa v0.7.12-r1039	Wellcome Trust Sanger Institute	http://bio-bwa.sourceforge.net
Bedtools v2.25.0	University of Utah	https://bedtools.readthedocs.io/en/latest/

RESOURCE AVAILABILITY

Lead contact

Further information and request for resources and reagents should be directed to and will be fulfilled by the Lead contact, Songtao Jia (songtao.jia@columbia.edu).

Materials availability

The materials generated in this study is available upon request and will be shared without restriction.

Data and code availability

The accession number for the RNA-seq, MNase-seq, and ChIP-seq data reported in this paper are GEO: GSE159192.

EXPERIMENTAL MODEL AND SUBJECT DETAILS

A list of yeast strains used is provided in Table S1. Yeast strains containing *hht3-K9MK14R* or *hht1-K14R* were generated by a PCR-based module method. All other strains were published or constructed through genetic crosses.

METHOD DETAILS

Serial dilution analyses

For serial dilution plating assays, ten-fold dilutions of a mid log-phase culture were plated on the indicated medium and grown for 3 days at 30°C.

Chromatin immunoprecipitation (ChIP) analyses

Log-phase yeast cells grown at 30°C were incubated at 18°C for 2 hours and then fixed for 30 minutes in 3% freshly made formaldehyde. The cells were pelleted and washed with PBS (phosphate-buffered saline) before resuspended in ChIP lysis buffer (50 mM HEPES-KOH, pH 7.5, 140 mM NaCl, 1% Triton X-100, 0.1% Deoxycholate). Ice cold glass beads were added and the mixtures were vigorously disrupted in a beadbeater. The lysates were collected and subjected to sonication to reduce chromatin size to 500-1000 base pairs (bp). The cleared cell lysates were incubated with Flag-agarose beads (Sigma) overnight at 4°C. The beads were then washed with ChIP lysis buffer twice, ChIP lysis buffer containing 0.5 M NaCl, Wash buffer (10 mM Tris, pH 8.0, 250 mM LiCl, 0.5% NP-40, 0.5% Deoxycholate, 1 mM EDTA), and TE (50 mM Tris pH 8.0, 1 mM EDTA). The bound chromatin fragments were eluted with TES (50 mM Tris pH 8.0, 1 mM EDTA, 1% SDS), and the crosslinking was reversed by incubating at 65°C overnight. The protein DNA mixture was then subjected to proteinase K treatment and phenol:chloroform extraction before the DNA was precipitated by ethanol.

For TetR-Clr4 release, tetracycline was added to log-phase cultures at 30°C to a final concentration of 10 μM and samples were taken at 5, 10, and 20 minutes, fixed with 3% freshly made formaldehyde for 30 minutes at 18°C.

Quantitative real-time PCR (qPCR) was performed with Maxima SYBR Green qPCR Master Mix (Fermentas) in a StepOne Plus Real-Time PCR System (Applied Biosystems). DNA serial dilutions were used as templates to generate a standard curve of amplification for each pair of primers, and the relative concentration of the target sequence was calculated accordingly. An *act1* fragment was used as a reference to calculate the enrichment of ChIP over the whole-cell extract (WCE) for each target sequence. A list of DNA oligos used is provided in the Key resources table.

ChIP-seq

DNA samples were prepared according to TruSeq ChIP sample preparation guide (Illumina) and sequenced on the Illumina HiSeq 2500 system by 100-bp paired-end sequencing. The raw reads were trimmed by Trimmomatic (v0.35) to remove remaining adaptor contaminants and low-quality regions. The trimmed reads were aligned to the *S. pombe* reference genome (Ensembl assembly version: ASM294v2.29) by bwa (v0.7.12-r1039) (http://bio-bwa.sourceforge.net/). The read-mapping files were further processed by Samtools (v1.2) picard-tools (v2.0.1) (http://broadinstitute.github.io/picard/) and GATK (v3.5) for indexing, sorting, PCR duplicates removal, and local-realignment around Indels. The per-based mapping depth was calculated by bedtools (v2.25.0) and the sliding window analyses were further performed using a 100-bp window size and 50-bp step size. ChIP-seq data is available at GEO: GSE159192.

ChIP-seq of H3K9me3 in hht3-K9MK14R cells

Log-phase yeast cells were crosslinked with 1% formaldehyde for 20 minutes with shaking at room temperature, followed by 5 minutes quenching with 125mM glycine. Cells were harvested, washed with PBS (phosphate-buffered saline) and flashfrozen with liquid nitrogen. The thawed pellet was washed and then resuspended in ChIP lysis buffer (50 mM HEPES-KOH, pH 7.5, 140 mM NaCl, 1% Triton X-100, 0.1% Deoxycholate, 1mM PMSF). Ice-cold glass beads were added and the mixtures were vigorously disrupted in a bead-beater with four 30 s rounds. The lysates were collected and NP buffer was added (10 mM Tris, pH 7.4, 1 M sorbitol, 50 mM NaCl, 5 mM $MgCl_2$, 1 mM $CaCl_2$). MNase was added to the reaction and the reactions were incubated at 37°C for 20 minutes. MNase amount was titrated empirically so that the chromatin was digested to yield mainly mono- and di-nucleosomes. The reaction was stopped by the addition of 0.5 M EDTA, and the tubes were placed on ice. 5X ChIP lysis buffer was added to the reaction, mixed by short vertexing, and the tubes were incubated on ice for 30 minutes. The reactions were then cleared by centrifugation at 16,000 x *g* for 10 minutes. A small fraction of the cleared supernatant was reserved as input and the rest was used for immunoprecipitation. The protocols for immunoprecipitation, reverse-crosslinking, and DNA precipitation are the same as in the previous ChIP section. The precipitated DNA was treated with RNAase A (EN0531, Thermo Fisher Scientific) for 1 hour at 37°C. DNA concentration was determined with the Qubit dsDNA HS Assay Kit (Q33230, Thermo Fisher Scientific). 1-5 ng of ChIP and input DNA were used for library construction using the NEBNext Ultra II DNA Library Prep Kit for Illumina (E7645, NEB). Libraries were pooled and sequenced with single-end sequencing on a NextSeq500/550 at the JP Sulzberger Genome Center at Columbia University.

Sequencing reads were de-multiplexed and aligned to the *S. pombe* reference genome (ASM294v2), obtained from Pombase (Lock et al., 2019) with Bowtie2 using default parameters (Langmead and Salzberg, 2012). Genome-wide coverage was calculated with deepTools2 (Ramírez et al., 2016) and normalized to counts per million (CPM). The coverage plot was visualized with IGV (Robinson et al., 2011). ChIP-seq experiments were performed in duplicates for each genotype.

RNA analyses

Total cellular RNA was isolated from log-phase cells using MasterPure yeast RNA purification kit (Epicenter) according to the manufacturer's protocol. qRT-PCR analyses were performed with Power SYBR® Green RNA-to-CT 1-Step Kit (Thermo Fisher Scientific) in a StepOne Plus Real-Time PCR System (Applied Biosystems). RNA serial dilutions were used as templates to generate a standard curve of amplification for each pair of primers, and the relative concentration of the target sequence was calculated accordingly. An *act1* fragment served as a reference to normalize the concentration of samples. The concentration of each target gene in wild-type cells was arbitrarily set to 1 and served as a reference for other samples. A list of DNA oligos used is provided in STAR Methods.

Western blot analyses

Cell lysates were prepared by lysing yeast cells with a beadbeater in ChIP lysis buffer. The lysates were sonicated for a total of 10 minutes to fragment chromatin. The cleared lysates were mixed with 2xSDS loading dye and resolved by SDS-PAGE. Western blot analyses were performed with Flag (Sigma), GFP (Covance), and Tubulin antibodies.

Generation of peptides containing H3K14ub mimics

Histone H3 tail peptides with a C-terminal biotinylated lysine, H3K14C (residues 1–21, ARTKQTARKSTGGCAPRKQLAGGK-biotin) and H3K9MK14C (ARTKQTARMSTG GCAPRKQLAGGK-biotin) were synthesized by Biomatik. Recombinant 6xHis tagged Ub-G76C was purified from *E.coli* using Talon beads according to manufacturer's protocol (Takara). Peptides and Ub-G76C were mixed in a buffer of 50 mM Borate pH 8.1, 2 mM TCEP to a final concentration of 200 μM peptide and 100 μM Ub. The mixture was incubated

at 37°C for 30 minutes and cool on ice for additional 30 minutes. Freshly made DCA was added to a final concentration of 100 μM and the mixture was incubated on ice for 1 hour. The reaction is quenched by the addition of 5 mM mercaptoethanol.

The reaction mixture was first purified with an ULTRA-15ml centrifugal filter (10KDa cutoff, Amicon) to remove unreacted peptides and self-ligated peptides, and then further purified with Avidin agarose column (Thermo Scientific). The column was washed with PBS first, and then blocked with Biotin Blocking/Elution Buffer (2 mM D-biotin in PBS). After washing with Regeneration buffer (0.1M glycine, pH 2.8) and PBS, samples were loaded onto the column, and the column was then washed with PBS. H3K14ub mimics were eluted with Regeneration buffer.

Protein expression and purification

The SET domain of recombinant Clr4 (residues 190-490) and the 3FA mutant were cloned into a pET28a vector. The expression plasmids were transformed into Rosetta cells and protein expression was induced using 0.15 mM isopropyl-1-thio-D-galactopyranoside. After incubation overnight at 16 C, the cells were harvested and resuspended in lysis buffer (50 mM sodium phosphate, 300 mM NaCl, pH 7.0), supplemented with 2 mM β-mercaptoethanol and lysed with ultrasonication. The lysate was incubated with Talon metal affinity resin (Takara Bio USA) and then washed with lysis buffer containing 15 mM imidazole. Bound protein was eluted with lysis buffer containing 150 mM imidazole.

Peptide binding assays

Protein binding assays were performed by incubating recombinant proteins with biotinylated histone peptides in binding buffer (10mM Tris, 150 mM NaCl, 1mM EDTA, 1mM DTT, 10 μM SAM, 0.05% NP-40) for one hour at 30°C. Streptavidin beads were added to isolate biotinylated peptide and associated proteins. The beads were washed four times in binding buffer. The proteins bound to the beads were resolved by SDS-PAGE and stained with Coomassie blue.

Thermal shift assay

The thermal stability of the SET domain of clr4 with ligands was analyzed at various temperatures using the Mx3005 P Real-Time PCR system (Stratagene). Purified Clr4-SET or Clr4-SET-3FA mutant (3 μM) protein was incubated with 20 μM of H3K14C peptide, H3K9MK14C, H3K14ub, or H3K9MK14ub, in the presences of 150 μM of SAM. All assays were performed in duplicate for each sample and contained final concentrations of 50 mM Tris (pH 8.0), 1 mM EDTA and 0.5 mM DTT. Reactions were first incubated at room temperature for 10 minutes, then on ice for 10 minutes, and mixed with the fluorescence dye (SYPRO orange; Invitrogen). The temperature was increased from 25 to 99 °C in 1 °C intervals over a 75-min period. Fluorescence values for each curve were normalized to the maximum and the minimum of the curve.

Biolayer interferometry

BLI analyses were performed in black 96-well plates (greinerbio-one, Germany) on an OctetRED96 instrument (ForteBio, USA). Prior to use, biosensors were soaked in assay buffer (1X PBS, 0.01% NP-40, 0.5 mM DTT, and 0.2 ug/ml BSA) for 10 min. BLI assays consisted of six steps, all performed in the assay buffer: initial baseline (30 s), loading (120 s), and quenching (120 s), baseline (60 s), association (30 s), and dissociation (90 s). Each biotinylated peptide (3 μg/ml) was immobilized on the Streptavidin biosensor tip during the loading step. To quench free streptavidin, 4 μg/ml of biocytin (Sigma), a biotin analog, was used. During the association step, analyte (Clr4-SET WT or 3FA mutant) at various concentrations was diluted into the assay buffer. Biotinylated-peptide-loaded sensors itself was measured as a control to subtract from experimental values before data processing. Sensorgrams were fit using global/1:1 binding model by ForteBio Data analysis version 10.0.1.6, from which the equilibrium dissociation constant (K_d) and association (k_{on}) and dissociation (k_{off}) rate constants were calculated. To measure the interaction in the presence of SAM, the assay buffer in all steps was supplied with 10 μM SAM.

In vitro histone methyltransferase assays

Histone methyltransferase assays were performed with recombinant Clr4 SET domain (25 nM), histone H3 tail peptide (residue 1-21) (1 μM) in histone methyltransferase buffer (10 mM Tris, pH 8.0, 1 mM EDTA, 1 mM DTT, 2 μM SAM) containing ^{3}H-SAM (400 nM) for 30 minutes at 25°C. The samples were resolved by SDS-PAGE and subjected to Coomassie staining to visualize the proteins and then treated with EN3HANCE (Perkin Elmer) to visualize labeled substrates.

For non-radioactive histone methyltransferase assays, recombinant Clr4 SET domain (50 nM) were incubated histone H3 tail peptide (residue 1-21) (10 μM) in histone methyltransferase buffer (10 mM Tris, pH 8.0, 1 mM EDTA, 1 mM DTT, 10 μM SAM) for 60 minutes at 25°C. The production of SAH was measured by the MTase-Glo Methyltransferase Assay kit according to the manufacture's protocol. Luminescence was measured using a Synergy Neo2 Microplate reader (BioTek Instruments).

QUANTIFICATION AND STATISTICAL ANALYSIS

For ChIP-qPCR, qRT-PCR, and HMTase assays, data are presented as mean ± SD with the number of technical replicates indicated.